Single Electron Bipolar Conductance Switch Driven by the Molecular Aharonov–Bohm Effect

Joonhee Lee, Nicholas Tallarida, Laura Rios, Shawn M. Perdue, and Vartkess Ara Apkarian*

Department of Chemistry, University of California, Irvine, California 92697-2025, United States

ABSTRACT

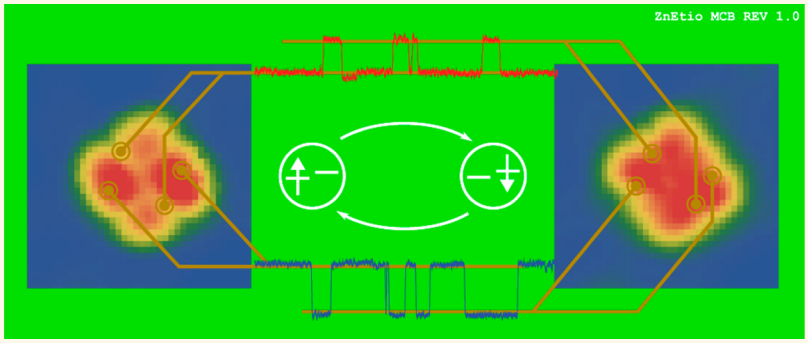

We demonstrate a conductance switch controlled by the spin-vibronic density of an odd electron on a single molecule. The junction current is modulated by the spin-flip bistability of the electron. Functional images are provided as wiring diagrams for control of the switch's frequency, amplitude, polarity, and duty-cycle. The principle of operation relies on the quantum mechanical phase associated with the adiabatic circulation of a spin-aligned electron around a conical intersection. The functional images quantify the governing vibronic Hamiltonian.

KEYWORDS: Jahn–Teller effect · molecular Aharonov–Bohm effect · spin-vibronic coupling

Ever since the original proposal of molecular electronics,[1] whereby single molecules act as functional circuit elements, there have been significant advances both in theoretical concepts[2] and experimental demonstrations.[3,4] Single molecule transistors,[5] rectifiers,[6] and switches[7−11] are among the demonstrated examples. The field is driven by the push to miniaturize electronics. To reach the promised very-large-scale integration, it is also essential to minimize heat generation through dissipative channels that may accompany the function of a circuit element. Conductance switching, namely the control of electron transport across a junction, can be regarded as the universal element of such circuitry. Conductance controlled through the movement of one atom has already been demonstrated.[10,11] The logical progression in miniaturization is an architecture in which conductance is controlled by the function of a single electron on a single molecule, with dissipation suppressed by eliminating moving parts. Here, we report on the realization of this limit.

We take advantage of the spin-flip bistability of an unpaired, Jahn–Teller (JT)-active electron on a single molecule to demonstrate a multithrow, bipolar, conductance switch. Our design rests on the recent demonstration that the vibronic density of an electron, subject to the dynamic JT-effect, determines its constant current topography in scanning tunneling microscopy (STM).[12] We show that the vibronic density can be dynamically manipulated through the electron's spin degree of freedom. The change in topography attendant to the spin-flip serves to control modulated current across the molecular junction, obviating the need for moving parts. The polarity of the conductance switch—positive, negative and neutral—is controlled by distinct contacts spaced within the molecule. We provide functional images

* Address correspondence to aapkaria@uci.edu.

Received for review April 4, 2014 and accepted May 13, 2014.

Published online May 13, 2014
10.1021/nn501875m

© 2014 American Chemical Society

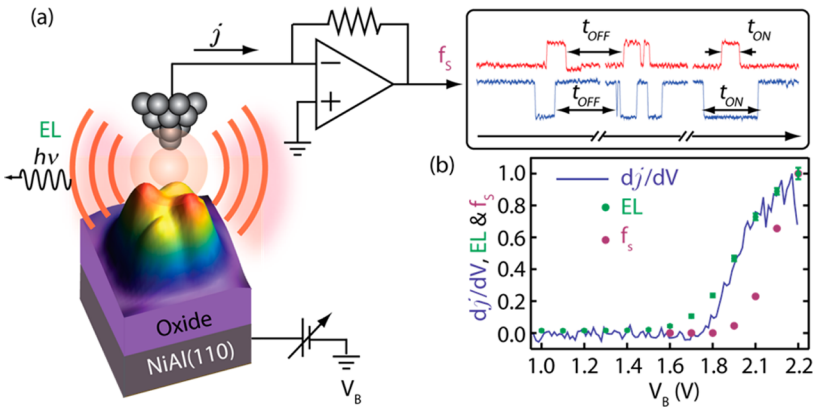

Figure 1. ZnEtio$^-$ as a light-emitting, conductance switch. (a) The time traces of the tunneling current show positive (red) or negative (blue) switching, depending on tip placement inside the molecule. (b) The normalized differential conductance curve, d*j*/d*V* *vs* *V* (blue curve), shows the onset of the dianion resonance near 1.8 eV. The photon count (green dots) and switching frequency (purple dots) track the same resonance.

as wiring diagrams for control of the operation of the switch.

Fundamentally, the implementation relies on the molecular Aharonov–Bohm (AB) effect. The term was coined by Mead,[13] recognizing the mathematical identity between the dynamical JT-effect introduced by Longuet-Higgins,[14] and the quantum phase of current on a vector potential, such as around a magnetic flux, considered by Aharonov and Bohm.[15] The unified origin of the two effects was later given through the construct of the geometric phase.[16,17] An insightful review of the experimental demonstrations of the AB-effect[18] and a perspective on the broad consequences of the geometric phase in molecular physics[19] have been given. The dynamic JT effect arises from the sign change accompanying adiabatic motion along a path that encircles the conical intersection of two potential energy surfaces.[20] To ensure reality, pseudospin states with fractional quantum numbers are introduced, and the potential separates into two adiabatic sheets forming a "Mexican hat".[14] The original treatment neglected electron spin. In the limit of strong spin–orbit coupling, the JT-effect disappears.[21] Important consequences, such as the breaking of Kramers degeneracy of half-odd states, occurs in the intermediate coupling regime.[22] In the limit of weak spin–orbit coupling, the spin-vibronic interaction becomes important. We show that despite the small interaction energy, 1 meV, spin-vibronic and pseudospin coupling splits the lower surface of the Mexican hat into two sheets, breaking the degeneracy of the $\pm 1/2$ states in the absence of external magnetic fields. The spin-flip induced by resonant scattering of tunneling electrons drives the transfer between the two sheets. The functional maps now allow the reconstruction of the spin-vibronic densities and the controlling Hamiltonian.

RESULTS AND DISCUSSION

The switch is illustrated in Figure 1. It consists of a single Zn-etioporphyrin radical anion (ZnEtio$^-$) isolated in the double-barrier junction of a cryogenic UHV-STM at 5 K and 2×10^{-11} Torr. The details of sample preparation and the instrument have been reported previously.[12] Briefly, ZnEtio$^-$ is prepared on a thin (5 Å) aluminum oxide layer grown on an atomically flat NiAl(110) substrate. The neutral molecule is sublimed on the prepared oxide, and subsequently reduced by injecting an electron at a bias of $V_b > 0.7$ V. Once charged, the anion remains stable as long as the junction bias is maintained above $V_b \sim -0.5$ V. The topographic image of the anion is shown in Figure 1. Its apparent shape is the constant current surface, which can be rigorously understood and reproduced in terms of the governing JT Hamiltonian, in the operative $E \otimes (b_1 \oplus b_2)$ symmetry:[20] The unpaired electron is in the doubly degenerate $E_g(x \pm iy)$ orbital, which in D_{4h} symmetry of the porphyrin ring is stabilized by coupling to skeletal deformations of rectangular $b_1(x^2 - y^2)$ and rhombic $b_2(xy)$ symmetry. The dynamic JT limit prevails, in which the pseudorotation of the skeleton drags the orbital into orbit. The nodal pattern of the b_1 state leads to the four-lobe appearance of the vibronic density. The uneven height of the lobes, to which we refer as big lobe (BL) and small lobe (SL), is due to crystal field splitting.[12] Upon ramping the junction bias, in addition to electroluminescence,[23,24] bistable current switching is observed to follow the differential conductance curve (d*j*/d*V*), as illustrated in Figure 1. The two phenomena share the same threshold, $V_b \sim 1.8$ V, which corresponds to access of the ZnEtio^{2-} dianion states and the opening of the conduction band of the oxide. A detailed analysis of the electroluminescence was given recently.[24] The process is assigned to radiative ionization of the dianion:

$$\mathrm{ZnEtio}^- + \mathrm{e}^-(2\mathrm{eV}) \rightarrow \mathrm{ZnEtio}^{2-} \rightarrow \mathrm{ZnEtio}^- + \mathrm{e}^- + \hbar\omega \quad (1)$$

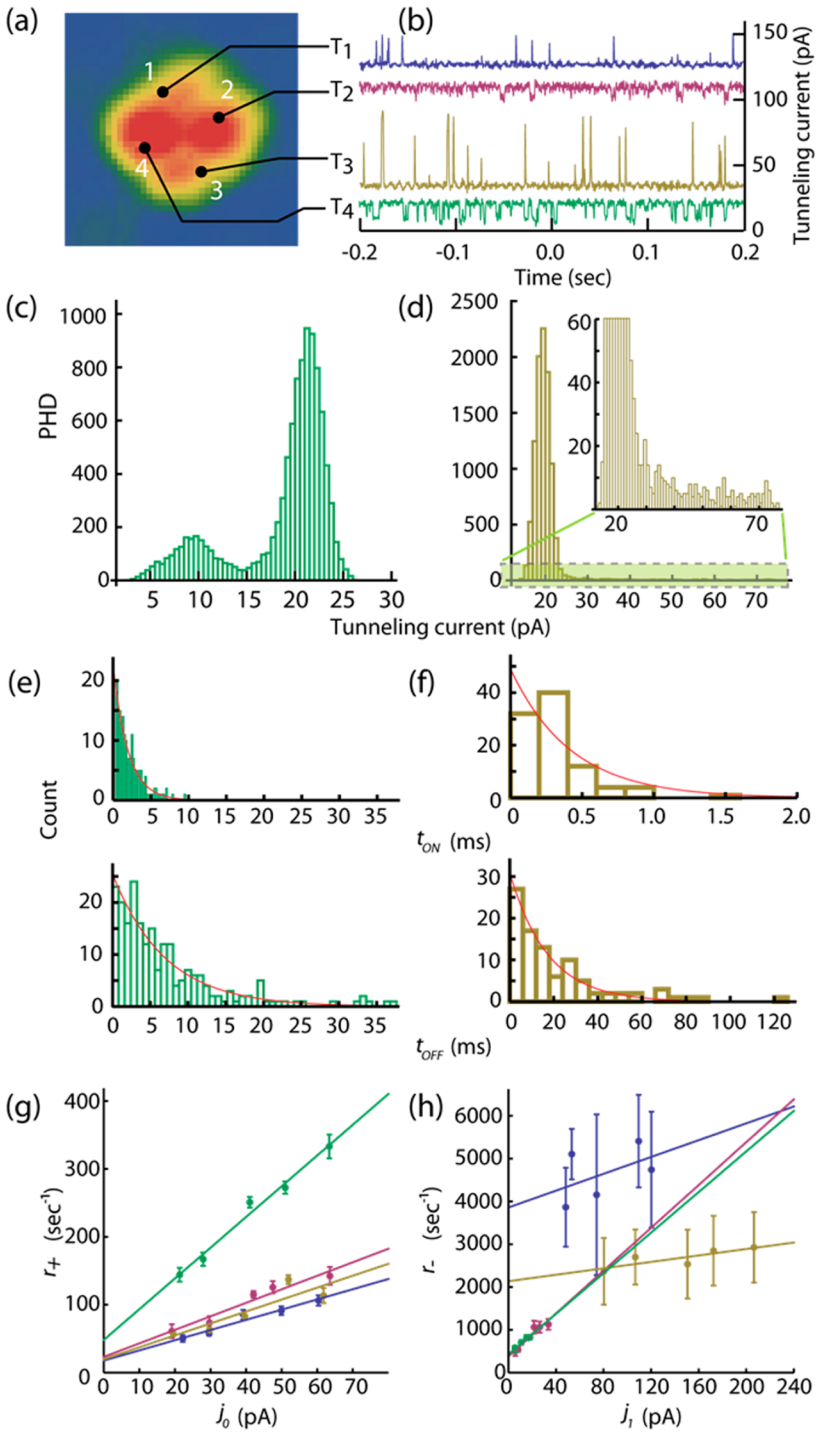

Figure 2. Reduction of the data. Time-traces recorded at j_0 = 20 pA and V_b = +2.2 V, on the four numbered contacts in (a) are shown in (b). The contact points are off-centered from individual lobes to maximize the switching activity as illustrated in Figure 3b. The traces are vertically offset for clarity. (c) Bimodal pulse height distribution at T_4 identifies dichotomous negative switching. (d) The PHD at T_3 shows a distribution of "on" states amplitudes, due to response time limitation. (e and f) Histograms of on/off-time distributions at T_4 and T_3 show Markovian distributions evidenced by their exponential fits. (g and h) The linear current dependence of the extracted transition rates, $r_{+/-} = 1/\tau_{0/1}$: (g) r_+ *vs* j_0 and (h) r_- *vs* j_1.

The bistable current fluctuations that accompany the same resonance, highlighted in Figure 1, constitute the conductance switch that we outline below.

Switching Kinetics. Figure 2 summarizes the essential data that characterizes the switching kinetics. We present time traces of current recorded (with feedback turned off, at V_b = 2.2 V) at four different tip placements, T_1–T_4, within the molecule (Figure 2a,b). We see pulse trains, characteristic of telegraph noise. When we define the DC set point as the "off" ≡ 0 state

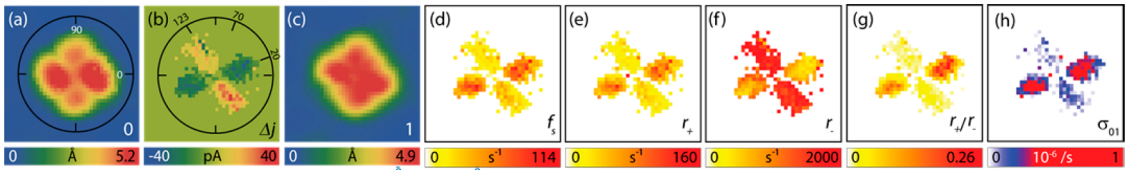

Figure 3. Functional images: (a) 42 Å × 42 Å topography of the 0-state, at j_0 = 20 pA; (b) the switching amplitude, δj; (c) topography of the 1-state; (d) switching frequency; (e) on-rate (r_+); (f) off-rate (r_-); (g) duty cycle (r_+/r_-); (h) stimulated transition probability σ_{01} map.

and the transient state as the "on" ≡ 1 state, the switching kinetics for a given single point measurement can be summarized by first-order kinetics:

$$0 \rightarrow 1; \quad r_+ = j_0\sigma_{01} + k_{01} \tag{2a}$$

$$1 \rightarrow 0; \quad r_- = j_1\sigma_{10} + k_{10} \tag{2b}$$

where $j_{0/1}$ is the current (electrons s^{-1}) in the off/on state, σ_{nm} is the probability for a tunneling electron to induce the transition from state n to m, and k_{nm} is the spontaneous switching rate constant (s^{-1}). The switching amplitude is a function of tip placement:

$$\delta j(x, y) \equiv j_1(x, y) - j_0 \tag{3}$$

with negative polarity, $\delta j < 0$, on the big lobes ($T_{2,4}$), and positive polarity, $\delta j > 0$, near the small lobes ($T_{1,3}$), as seen in Figure 2b. Where switching frequencies are within the gain-bandwidth of the current preamplifier (800 Hz, at 10^{10} gain), the observed pulse height distribution (PHD) is bimodal, as exemplified by the amplitude histogram recorded at T_4 in Figure 2c. Otherwise, it is necessary to correct for instrumental response to obtain the true height and "on"-time of the pulses. This is accomplished by a piece-wise deconvolution of the pulse shapes (see Supporting Information section 1). The apparent PHD recorded at T_3, illustrated by the histogram in Figure 2d, is such an example. The response time corrected signal shows bimodal distribution. This is more directly verified by reducing the bias, or the current set point, to reduce the switching frequency. For all tip placements, the corrected PHD appears bimodal, the local density of states is bistable, therefore the process is characterized as dichotomous.

When the PHD is used to discriminate between on/off states, the generated histograms of the residence times (Figure 2e,f) show exponential probability densities, $P_{0/1}$, characteristic to Markov processes:[25]

$$P_{0/1} = 1/\tau_{0/1}\exp(-t/\tau_{0/1}), \quad r_{+/-} \equiv 1/\tau_{0/1} \tag{4}$$

The rates, $r_{+/-}$, extracted from the fits to the residence time distributions, are linear functions of current, $j_{0/1}$, with slope and intercept that determine σ_{nm} and k_{nm}, respectively (Figure 2g,h). The extracted stimulated and spontaneous probabilities for on/off transitions at the four measured points are collected in Table 1. The data is representative of the same measurements carried out on 10 different molecules of similar topography.

TABLE 1. Stimulated Transition Probability per Electron (σ) and Spontaneous Rate Constant (k)

tip position	σ_{01} ($\times 10^{-6}$/e)	σ_{10} ($\times 10^{-6}$/e)	k_{01} (s^{-1})	k_{10} (s^{-1})
T_1	0.24	1.57	18.33	3859.07
T_2	0.32	4.00	23.25	383.31
T_3	0.28	0.60	19.84	2136.23
T_4	0.73	3.80	48.26	428.36

Inspection of Table 1 shows that there is a finite probability for the system to spontaneously switch-on: $k_{01} \sim 27 \pm 14\ s^{-1}$, as determined by the asymptotic limit $j \rightarrow 0$. The spontaneous relaxation rate back to the ground state yields a consistent value on the BLs ($T_{2,4}$): $k_{10} = 400 \pm 30\ s^{-1}$. However, k_{10} values recorded near the SLs ($T_{1,3}$) are an order of magnitude larger and show greater sensitivity to topography and variation from molecule to molecule. Having established that the kinetics is that of a two-level system, a single spontaneous lifetime would be expected for the excited state. We recognize that the systematic variation in k_{10} is due to perturbation by the tip. Where the switching polarity is positive and the local density of states expands against the tip, Pauli repulsion can be expected to raise the potential energy. The effect on the energy level is small. On the basis of the measurements on the BLs, assuming equal degeneracy, the energy difference between the two levels can be obtained by recourse to detailed balance:

$$\Delta E = k_B T \ln(k_{10}/k_{01}) = 1.3\,\text{meV} \tag{5}$$

The measurement on T_1 yields $\Delta E = 2.3$ meV, establishing that the tip perturbation is of the same order of magnitude, ~1 meV. Despite the small magnitude of the effect, the attendant change in topography is clearly observable through STM. This is the hallmark of topography determined by vibronic density.[12] We exploit the effect of topography on electron transport, to control current at the molecular junction.

Functional Imaging. A direct connection between vibronic structure and dynamic function can be made through images generated by measurements on a grid. These are presented in Figure 3. The maps are extracted from an extensive data set consisting of 0.5 s-long current traces digitized every 500 μs, recorded on a 38 × 38 spatial grid. The analysis procedure illustrated in Figure 2 is followed for each trace. We highlight the information content of the maps,

which may be regarded as wiring diagrams for control of the single electron switch.

The amplitude map, $\delta j(x,y)$, is signed (Figure 3b). Relative to the polar coordinate locked to the image of the "off" state (Figure 3a), the switching polarity changes continuously from positive, to neutral, to negative, between $\theta = 120°$, 70°, and 20°, respectively. The coarse grain image identifies a single-pole triple-throw bipolar rotary switch.

Given the topographic image of the "off" state and the switching amplitude map, the topography of the "on" state can be reconstructed as the constant current surface at the set point j_0:

$$Z_1(x,y)|_{j_0} = Z_0(x,y)|_{j_0} - \frac{1}{2\kappa}\ln\left(\frac{j_0+\delta j(x,y)}{j_0}\right) \quad (6a)$$

for tunneling current given as

$$j = j_0 \exp(-2\kappa(z - z_0)) \quad (6b)$$

in which j_0 is the current at the reference point $z = z_0$, and $\kappa = 1$ Å^{-1} is used. The extracted image of the excited state (Figure 3c) reveals a vibronic density rotated relative to ground state (Figure 3a), now with nearly equal lobes.

Functional images of directly observable dynamical variables: switching frequency, transition rates, r_+ and r_-, and duty cycle r_+/r_- are shown in Figure 3d–g. These apply to measurements carried out at one set point j_0 = 20 pA. The derived current independent switching probability map, which is an explicit function of the bias, $\sigma_{01}(x,y;V_b)$ is shown in Figure 3h. Together with the amplitude map (Figure 3b) and the relation eq 6a, the maps are sufficient to predict and control the function of the conductance switch—frequency, amplitude, polarity, and duty-cycle—by making selective contacts within the single molecule. More fundamentally, Figure 3a,c maps out the vibronic densities of the initial and final state, $\psi_0^*\psi_0$ and $\psi_1^*\psi_1$, while Figure 3h maps out the transition matrix element $|\langle 1|\sigma(x,y)|0\rangle|^2$ that connects states 0 and 1. Analytic expressions for the maps can be formulated in terms of the underlying vibronic Hamiltonian, which we consider next.

Vibronic Hamiltonian. The kinetic analysis establishes the switching as a dichotomous Markovian process with both forward and reverse transitions stimulated by resonant tunneling current. The small, 1 meV, energy difference between the two states, and the long lifetime of the excited state, $1/k_{10}$ = 1 ms, immediately suggest the transition to be the spin-flip of the odd electron. The spin–orbit coupling of π-electrons is small. A splitting of 0.1 meV has been estimated for ZnEtio$^-$.[26] The coupling is enhanced through vibrational distortions;[27] and near conical intersections, vibronic splittings of order 1 meV are obtained for small aromatics such as benzene and butadiene.[28] This is in line with the splitting we see, even though our measurement may be subject to tip and substrate perturbations. Although spin–orbit coupling in this weak coupling limit does not qualitatively change the JT Hamiltonian, the spin-vibronic coupling can be expected to generate spatially distinguishable densities. The entanglement between orbital angle and pseudorotation phase in the dynamic JT-effect allows reconstruction of the vibronic Hamiltonian from the measured topography of the electron density.[12] Thus, the ground state topography can be reproduced with the neglect of spin, using the Hamiltonian:

$$H = T + V = H_0 + \sum_i (\partial H_0/\partial Q_i)_0 Q_i \quad (7a)$$

in which H_0 is the electronic potential at the symmetric configuration, and the last term is the vibronic coupling. Casting V in established form:[29]

$$V = \frac{1}{2}k_1Q_1^2 + \frac{1}{2}k_2Q_2^2 + cQ_1Q_2 + aQ_1 + bQ_2 \pm \sqrt{\left(c_1Q_1+\frac{\delta_1}{2}\right)^2 + \left(c_2Q_2+\frac{\delta_2}{2}\right)^2} \quad (7b)$$

in which $c_{1,2}$ and $\delta_{1,2}$ represent the JT-coupling and crystal field splitting parameters, respectively; the coupling between modes, cQ_1Q_2, is necessary to reproduce the observed chirality of the density, and the tilt of the conical intersection is controlled by the slopes a, b. The energy scale is established by the active vibrations, through the force constants, $k_{1,2}$. The vibronic eigenstates are the doubly degenerate pseudospin states $\Psi = \psi\, e^{im\phi}$ with $m = \pm 1/2, \pm 3/2, \ldots$, as derived originally.[14]

Inclusion of electron spin modifies the Hamiltonian:

$$H = H_0 + H_{SO} + \sum_i \{(\partial H_0/\partial Q_i)_0 + (\partial H_{SO}/\partial Q_i)_0\} Q_i \quad (8)$$

with three terms that describe spin–orbit, vibronic, and spin-vibronic coupling, in order. In the weak coupling limit, the bare H_{SO} doubles the degeneracy of states, and adds a constant under the radical in eq 7b, but does not change the level structure; while the spin-vibronic coupling modifies the effective coupling constants, c_1 and c_2 in eq 7. With the adjustment of parameters and the classical inversion of the spin-vibronic potential, $\rho = \exp(-V/E_{1/2})$, the observed topographies of ground and excited state can be nicely reproduced, as shown in Figure 4. The used parameter set is given in Table S2 of Supporting Information. The fitting parameter, $E_{1/2}$, which plays the role of zero-point energy, when scaled by the previously identified vibrational energy of the JT active deformation E_v = 20 meV, yields the energy splitting of $E_v(E_{1/2,1} - E_{1/2,0}) \sim 1$ meV, in good agreement with the experiment. A consistent interpretation of the observed densities in the 0 and 1 states and their energy difference is obtained. Moreover, the inversion allows the reconstruction of the two adiabatic potential energy surfaces, which are shown in Figure 4 and which

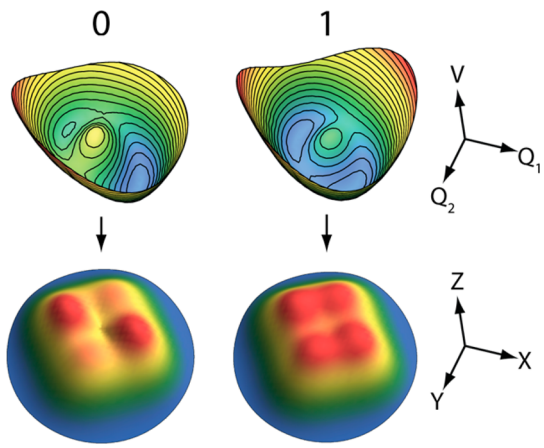

Figure 4. Adiabatic potential energy surfaces and density of the spin-vibronic states along the vibrational coordinates (Q_1, Q_2), and the observable electron densities they sustain along Cartesian coordinates.

completely specify the spin-coupled vibronic Hamiltonian. The wave functions are modified, $\Psi = \psi e^{il\phi}$ by inclusion of the spin, $l = m \pm s_z$, which shares the same quantization axis, z, as the pseudorotation. Each m-state is split by the spin-vibronic coupling, and in particular, the ground $m = \pm 1/2$ state is split into $l = \pm 0$, ± 1 states in which pseudospin and spin are counter-aligned and aligned, respectively. Two Zeeman active vibronic sequences of doubly degenerate states is obtained, as recently observed in magnesium porphyrin ions.[30] However, the original Kramers degeneracy between $m = \pm 1/2$ states is broken, and a spin-flip leads to the $0 \rightarrow 1$ transition.

That the spin-flip transition is resonantly induced by electrons that scatter on the dianion states (1), can be readily understood. Given ^2E_g parentage of the spin-aligned electron, the accessible dianion states are $E_g \otimes E_g = {}^1A_{1g} + {}^1B_{1g} + {}^1B_{2g} + {}^3A_{2g}$.[31] While the triplet state preserves spin alignment, scattering *via* the singlet states scrambles it (see Figure 5a). In our prior analysis of the electroluminescence, we derived the propensity rule that the injection of a second electron in the BLs leads to states of double occupancy, $e_g{}^2e_g$, while injection in the SLs leads to JT-inactive[1,3] A states of single occupancy e_ge_g.[24] Accordingly, based on a strictly statistical consideration, we would expect a spin-flip probability of 5:1 between BLs and SLs (isotropic probability for accessing the totally symmetric A-states, and access to $^1B_{1g}$ and $^1B_{2g}$ limited to the BLs). This is indeed near quantitative agreement with the switching probability map $\sigma_{01}(x,y)$ of Figure 3h. The small yield of the process, $\sim 10^{-7}$ per tunneling electron, renders the random telegraph noise character of switching.

Finally, we note that the spontaneous switching transitions, which dominate the $1 \rightarrow 0$ spin-flip relaxation, are expected to proceed without dissipation. Given the phonon bottleneck at 1 meV, the spin−lattice relaxation is forced *via* the Orbach process

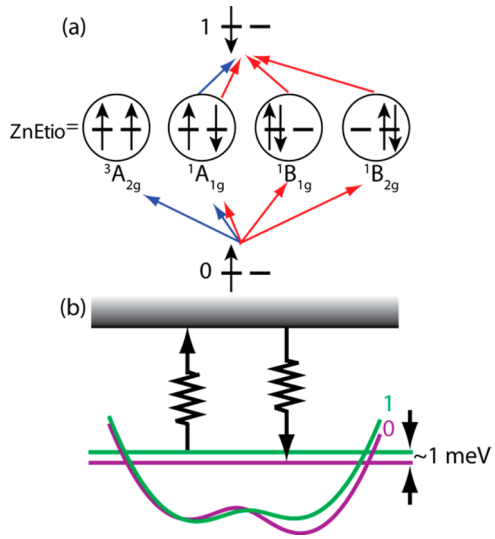

Figure 5. Stimulated and spontaneous transition mechanisms. (a) Spin-flipping *via* scattering of tunneling electrons on the dianion resonance. Triplet/singlet scattering channels on SL are indicated by blue arrows, and singlet scattering channels on BL are indicated by red arrows. (b) Spontaneous transition through the Orbach process.

depicted in Figure 5b.[32] The two-phonon process involves resonant absorption and emission, with optical phonons of the Al_2O_3 substrate most likely to serve as the resonance. Thus, the spontaneous transitions do not generate a thermal load. The main dissipative channel in the switch is the inelastic scattering of tunneling electrons that stimulate the spin-flip. This step is subject to rapid vibrational relaxation in the $ZnEtio^{2-}$ manifold, as verified by the vibrationally relaxed electroluminescence that accompanies the same scattering process. The ~2 eV energy of the injected electrons dissipate either through radiation or in the metal bulk after tunneling, over the scattering length scale. The load may be minimized by driving the transition near the threshold of the electronic resonance seen in Figure 1 but cannot be entirely eliminated. For electron transport in the weak-coupling limit of the STM junction, where typical currents do not exceed 10 nA, thermal effects are entirely negligible.

CONCLUSIONS

We illustrated that the vibronic density of a single electron may be used to control electron transport across a molecular junction, with minimal heat load. The dynamical information extracted from an extensive data set was presented through functional images. This direct connection between structure and function maps out the wiring diagram of the switch; alternatively, it maps out the molecular spin-coupled vibronic Hamiltonian. The demonstrated conductance switch relies on a distinctly quantum mechanical effect, namely the geometric phase associated with current encircling a singularity, as in the Aharonov−Bohm

effect. Here, the zero-point pseudorotation of the macrocycle drives the permanent circulation of the electron, with spin aligned by the motion. The phase accumulated by the quantum current around the singularity of the conical intersection depends on the spin projection and the sense of rotation. This has the effect of combining the fractional quantum numbers of the bosonic pseudospin and electron spin to break the Kramers degeneracy of the original $\pm 1/2$ states. Despite the small magnitude of the splitting (1 meV), the resulting spin-vibronic states are distinguished and quantified through their spatial densities $\psi^2(Q;q,s)$ which determine their STM topography. It should be possible to take full advantage of the quantum nature of the switch through spin-polarized STM, for controlled manipulation of the quantum bit of information stored in the switch.

METHODS

ZnEtio molecules were sublimed onto an aluminum oxide film grown on a NiAl(110) single crystal surface at 5 K. The adsorbed molecules on the oxide were subsequently reduced by injecting tunneling electrons at the bias larger than +0.7 V. We interrogated the ZnEtio anion molecules by recording the time traces of tunneling current and photon counts over a grid using a digital oscilloscope and avalanche photodiode combined with a photon counter. The obtained data were further processed through the statistical analysis to spatially map the functions of the molecular switch.

Conflict of Interest: The authors declare no competing financial interest.

Supporting Information Available: Deconvolution of pulse shapes and fitting parameters for the spin-vibronic potential. This material is available free of charge *via* the Internet at http://pubs.acs.org.

Acknowledgment. This research was made possible through the unique opportunities granted by the NSF Center for Chemical Innovation dedicated to Chemistry at the Space-Time Limit (CHE-0802913). We have greatly benefitted from discussions with M. N. van Staveren and J. A. Cina.

REFERENCES AND NOTES

1. Aviram, A.; Ratner, M. A. Molecular Rectifiers. *Chem. Phys. Lett.* **1974**, *29*, 277–283.
2. Ghosh, A. W.; Damle, P. S.; Datta, S.; Nitzan, A. Molecular Electronics: Theory and Device Prospects. *MRS Bull.* **2004**, *29*, 391–395.
3. Aradhya, S.; Venkataraman, L. Single-Molecule Junctions beyond Electronic Transport. *Nat. Nanotechnol.* **2013**, *8*, 399–410.
4. van der Molen, S. J.; Liljeroth, P. Charge Transport through Molecular Switches. *J. Phys.: Condens. Matter* **2010**, *22*, 133001–133030.
5. Martel, R.; Schmidt, T.; Shea, H. R.; Hertel, T.; Avouris, P. Single- and Multi-Wall Carbon Nanotube Field-Effect Transistors. *Appl. Phys. Lett.* **1998**, *73*, 2447–2449.
6. Aviram, A.; Joachim, C.; Pomerantz, M. Evidence of Switching and Rectification by a Single Molecule Effected with a Scanning Tunneling Microscope. *Chem. Phys. Lett.* **1988**, *146*, 490–495.
7. Donhauser, Z. J.; Mantooth, B. A.; Kelly, K. F.; Bumm, L. A.; Monnell, J. D.; Stapleton, J. J.; Price, D. W., Jr.; Rawlett, A. M.; Allara, D. L.; Tour, J. M.; *et al.* Conductance Switching in Single Molecules through Conformational Changes. *Science* **2001**, *292*, 2303–2307.
8. Moresco, F.; Meyer, G.; Rieder, K.-H. Conformational Changes of Single Molecules induced by Scanning Tunneling Microscope Manipulation: a Route to Molecular Switching. *Phys. Rev. Lett.* **2001**, *86*, 672–675.
9. Huang, M. T.; Zhao, J.; Feng, M.; Popov, A. A.; Yang, S.; Dunsch, L.; Petek, H. A Molecular Switch Based on Current-Driven Rotation of an Encapsulated Cluster within a Fullerene Cage. *Nano Lett.* **2011**, *11*, 5327–5332.
10. Kumagai, T.; Hanke, F.; Gawinkowski, S.; Sharp, J.; Kotsis, K.; Waluk, J.; Persson, M.; Grill, L. Controlling Intramolecular Hydrogen Transfer in a Porphycene Molecule with Single Atoms or Molecules Located Nearby. *Nat. Chem.* **2014**, *6*, 41–46.
11. Schrim, C.; Matt, M.; Pauly, F.; Cuevas, J. C.; Nielaba, P.; Scheer, E. A Current-Driven Single-Atom Memory. *Nat. Nanotechnol.* **2013**, *8*, 645–648.
12. Lee, J.; Perdue, S. M.; Rodriguez Perez, A.; El-Khoury, P. Z.; Honkala, H.; Apkarian, V. A. Orbiting Orbitals: Visualization of Vibronic Motion at a Conical Intersection. *J. Phys. Chem. A* **2013**, *117*, 11655–11664.
13. Mead, C. A. Electronic Spin-Orbit Interaction and the Molecular Aharonov-Bohm Effect. *Chem. Phys.* **1980**, *49*, 33–38.
14. Longuet-Higgins, H. C.; Opik, U.; Price, M. H. L.; Sack, R. A. Studies of the Jahn-Teller Effect II: The Dynamical Problem. *Proc. R. Soc. London, Ser. A* **1958**, *244*, 1–16.
15. Aharonov, Y.; Bohm, D. Significance of Electromagnetic Potentials in Quantum Theory. *Phys. Rev.* **1959**, *115*, 485–491.
16. Berry, M. V. Quantal Phase Factors Accompanying Adiabatic Changes. *Proc. R. Soc. London, Ser. A* **1984**, *392*, 45–57.
17. Simon, B. Holonomy, the Quantum Adiabatic Theorem, and Berry's Phase. *Phys. Rev. Lett.* **1983**, *51*, 2167–2170.
18. Batelaan, H.; Tonomura, H. The Aharonov-Bohm Effects: Variations on a Subtle Theme. *Phys. Today* **2009**, *62*, 38–43.
19. Wittig, C. Geometric Phase and Gauge Connection in Polyatomic Molecules. *Phys. Chem. Chem. Phys.* **2012**, *14*, 6409–6432.
20. Bersuker, I. B. *The Jahn-Teller Effect*; Cambridge University Press: Cambridge, 2006; pp 52−62.
21. Ballhausen, C. J. Jahn-Teller Configuratioal Instability in Square-Planar Complexes. *Theoret. Chim. Acta* **1965**, *3*, 368–374.
22. Mead, C. A. Molecular Kramers Degeneracy and Non-Abelian Adiabatic Phase Factors. *Phys. Rev. Lett.* **1987**, *59*, 161–164.
23. Chen, C.; Chu, P.; Bobisch, C. A.; Mills, D. L.; Ho, W. Viewing the Interior of a Single Molecule: Vibronically Resolved Photon Imaging at Submolecular Resolution. *Phys. Rev. Lett.* **2010**, *105*, 217402.
24. Lee, J.; Perdue, S. M.; Rodriguez Perez, A.; Apkarian, V. A. Vibronic Motion with Joint Angstrom-Femtosecond Resolution Observed through Fano Progressions Recorded within One Molecule. *ACS Nano* **2014**, *8*, 54–63.
25. Gardiner, C. W. *Handbook of Stochastic Methods for Physics, Chemistry and the Natural Sciences*; Springer: Berlin, 1997; pp 42−79.
26. Gouterman, M.; Yamanashi, B. S.; Kwiram, A. L. Zero-Field Splitting of the Triplet State in Zinc Etioporphyrin. *J. Chem. Phys.* **1972**, *56*, 4073–3079.
27. McConnell, H. M. Spin-Orbit Coupling in Orbitally Degenerate States of Aromatic Ions. *J. Chem. Phys.* **1961**, *34*, 13–16.
28. Penfold, T. J.; Worth, G. A. The Effect of Molecular Distortions on Spin-Orbit Coupling in Simple Hydrocarbons. *Chem. Phys.* **2010**, *375*, 58–66.

29. Hoffman, B. M.; Ratner, M. A. Jahn-Teller Effects in Metalloporphyrins and Other Four-Fold Symmetric Systems. *Mol. Phys.* **1978**, *35*, 901–925.
30. Ham, U.; Ho, W. Spin Splitting Unconstrained by Electron Pairing: the Spin-Vibronic States. *Phys. Rev. Lett.* **2012**, *108*, 106803.
31. Cotton, F. A. *Chemical Applications of Group Theory*; John Wiley & Sons: New York, 1990; pp 98−104.
32. Orbach, R. Spin-Lattice Relaxation in Rare-Earth Salts. *Proc. R. Soc. London, Ser. A* **1961**, *264*, 458–484.